JOURNAL OF PROPULSION AND POWER
Vol. 18, No. 6, November–December 2002

Analysis and Application of Chorochronic Periodicity in Turbomachinery Rotor/Stator Interaction Computations

G. A. Gerolymos,* G. J. Michon,† and J. Neubauer‡
Université Pierre-et-Marie-Curie, 91405 Paris, France

A methodology for predicting the three-dimensional unsteady aerodynamics of the interaction between two turbomachinery blade rows that are in relative angular motion with one another is described. In this case, the kinematics of the blades introduce a chorochronic (space–time) periodicity. This periodicity is analyzed in detail, and a mathematically straightforward methodology, based on Fourier series in θ (azimuth) and t (time), is presented for treating the interface between the two rows. These results are implemented in a computational method solving the three-dimensional Favre–Reynolds-averaged Navier–Stokes equations, with a near-wall wall-normal-free Reynolds-stress model. Only one blade passage per blade row is discretized. At the pitchwise boundaries, phase-lagged periodicity is applied using Fourier series in time. Both the pitchwise boundaries time harmonics and the interface chorochronic $t\theta$ harmonics are updated using a low-storage moving-averages technique. Computational results are presented and compared with measurements for a $1\frac{1}{2}$-stage turbine, where the two stators have the same number of blades enabling the use of chorochronic periodicity. Sample results are also presented for a transonic inlet guide vane/rotor interaction, illustrating the ability of the interface treatment to handle shock waves.

Nomenclature

$\boldsymbol{c}$	=	vector of conservative variables in the Cartesian frame of reference [Eq. (16)]
DH	=	downstream H-type grid[41]
$\boldsymbol{F}$	=	time-periodic function (its argument is the phase)
f	=	frequency
H_R	=	rothalpy
ℓ_θ	=	nonzero circumferential-harmonics index [Eqs. (8)]
M	=	absolute Mach number
M_W	=	relative Mach number
m_t	=	time-harmonic number
$\dot{m}$	=	mass flow
N_B	=	number of blades of a blade row
N_{PP}	=	number of points per period of the numerical discretization
n_B	=	blade count in a blade row [Eq. (23)]
n_{BR}	=	blade-row index
n_t, N_t	=	time-harmonic number and harmonics retained in the Fourier series
n_θ, N_θ	=	circumferential-harmonic number and harmonics retained in the Fourier series
n_w^+	=	nondimensional distance of the first grid point from the wall, $nu_\tau \breve{\nu}_w^{-1}$ (where n is the distance from the wall, u_τ the friction velocity, and $\breve{\nu}_w$ the kinematic viscosity at the wall
O	=	O-type grid; O grid around the blades[41]
OZ	=	buffer O-type grid between TC and O[41]
P, P', Q_+, Q_-, M, M_1, M_2, M_3	=	grid points (Figs. 2 and 3)
p	=	pressure
$\Re$	=	real part of a complex number or function
TC	=	clearance-gap grid[41]
t	=	time
UH	=	upstream H grid[41]
$\boldsymbol{u}$	=	vector of variables [Eq. (15)]
V, v	=	absolute flow velocity and turbulent velocity fluctuation
$\boldsymbol{v}$	=	vector of nonconservative variables [Eq. (14)]
W, w	=	relative flow velocity and turbulent velocity fluctuation
$\boldsymbol{w}$	=	vector of flow variables
(x, R, θ)	=	cylindrical system of coordinates (x is the engine axis)
(x, y, z)	=	Cartesian system of coordinates (x is the engine axis)
α	=	absolute flow angle of the velocity vector from the local meridional direction
β_r	=	interblade phase angle (phase shift)
Δt	=	time step
ε^*	=	turbulence kinetic energy dissipation-rate
ρ	=	density
ς	=	normalized blade span, $\in [0, 1]$
Ω	=	rotational velocity of the blades

Subscripts

abs	=	absolute frame of reference
ISA	=	standard conditions (International Standard Atmosphere at sea level)
M	=	pitchwise averaged quantities (meridional)
MF	=	mean flow (Favre–Reynolds-averaged quantities)
T	=	turbulent
t	=	total thermodynamic quantities; time
W	=	relative
w	=	wall
x, R, θ, y, z	=	vector or tensor components along the corresponding coordinate
1, 2	=	blade-row indices

Received 10 September 2001; revision received 14 March 2002; accepted for publication 3 April 2002.

*Professor, Director, Laboratoire d'Energétique, Unité Associée au Centre National de Recherche Scientifique, Bâtiment 511, Orsay.

†Research Engineer, Laboratoire d'Energétique, Unité Associée au Centre National de Recherche Scientifique, Bâtiment 511, Orsay.

‡Research Assistant, Laboratoire d'Energétique, Unité Associée au Centre National de Recherche Scientifique, Bâtiment 511, Orsay.

Superscripts

n	=	time level of the numerical discretization
T	=	transpose
$\tilde{}$	=	Favre average
$''$	=	Favre fluctuations
$\bar{}$	=	Reynolds average (ensemble average)
$\breve{}$	=	function of averaged quantities that is neither a Favre average nor a Reynolds average
$\hat{}$	=	chorochronic harmonics (complex numbers)
$\check{}$	=	time harmonics (complex numbers)

Introduction

THE prediction of the unsteady aerodynamic interaction between adjoining blade rows is an important problem in turbomachinery analysis, especially in relation to the interaction with upstream wakes[1,2] or shock waves.[3] The straightforward computation of the flowfield by modeling all of the blades in each blade row is computationally very expensive. Most authors model a limited number of blades in each blade row and modify the number of blades in each row (eventually adjusting the chords to get the correct solidity) to recover space-periodic conditions at the pitchwise boundaries of the domain.[4–12] Arnone and Pacciani[13] have compared various modifications of the blade numbers with the results obtained for the correct blade numbers (using a two-dimensional Navier–Stokes solver) and concluded that serious inaccuracies can be introduced by blade count modifications techniques. Furthermore, such techniques prohibit the coupling of the unsteady aerodynamic results with acoustic propagation techniques because the propagation of acoustic modes is very sensitive to the number of circumferential lobes.[14]

A few authors[15–27] (Table 1, see also Ref. 28) prefer exploiting the chorochronic periodicity (where choros refers to space and chronos to time) characterizing the motion of the blades.[29] The knowledge of this periodicity is traceable to the early work of Kemp and Sears[30] and to the well-established theory of Tyler and Sofrin[14] for acoustic modes propagation in turbomachinery ducts. If the two blade rows are isolated from other neighbors, and are in relative angular motion, then the fundamental unsteady frequency in the frame relative to each blade row is the blade passing frequency (BPF) of the blades of the adjacent blade row. Furthermore, each blade in a given row observes the same flow phenomena as the neighboring blade in the same row, but with a phase shift determined by the ratio of the numbers of blades between the two blade rows (circumferentially traveling wave). The only restrictive hypothesis is that aerodynamic instabilities, such as vortex shedding from thick trailing edges[31,32] or rotating stall,[33–35] are absent because such phenomena have their own frequency (asynchronous with the rotational velocity). The use of the chorochronic periodicity allows the computation of the flow around only one blade per blade row, using appropriate phase-shifted boundary conditions at the pitchwise boundaries.

There are two different approaches for numerically implementing the chorochronic periodicity: The first is the method introduced by Erdos et al.[15] that stores time signals (either for a number of instants per period or using a time Fourier series representation[36]) at each grid point at the pitchwise boundaries and at the computational interface between the two blade rows and uses these signals to reconstruct the flowfield at pitch-shifted positions using the appropriate time shift. The second is the method of applying a space–time transformation ($t' = t'[t, \theta]$) to the equations, introduced by Giles,[37] known as the time-inclining or time-tilting technique.

As far as the interface is concerned, for phase-lagged methods, most authors use quite complicated storage and interpolation techniques.[15–17] This could be considered a drawback of the phase-lagged method because time-inclining procedures, that travel with the wave in each frame of reference, only require space interpolation at the interface.[18,23] These interpolations, however, require specific shearing-cells techniques.[18]

There is a strict mathematical equivalence between the two techniques (time lag[15] and time inclining.[37]) Nonetheless, the time-inclining technique presents two drawbacks: 1) It presents severe numerical stability problems if the blade numbers ratio is much higher than unity.[5,12,18,23] (In which case more than one channel is modeled in the high blade count row.) 2) Each grid point in the computational grid is at a different physical time than its neighbors, so that obtaining a snapshot of the flow at a given instant requires storage and reconstruction techniques, even for the reference blade.[5] In the authors' opinion, this last drawback is a major one. For these reasons, the authors believe that the Fourier-based storage technique is the best choice because it uses a solver in the actual time–space and, as is shown in the present paper, can be implemented using an elegant interface treatment.

The purpose of this paper is to analyze the chorochronic periodicity properties, both for the pitchwise boundaries and the computational interface. A mathematically simple (and, as a consequence, easy to program) representation of the computational interface is

Table 1 Blade-row interaction computations using chorochronic periodicity

Ref.	Year	Two-dimensional/ three-dimensional	Closure	Technique	Application	$N_{B_i} : N_{B_{i+1}}$
Erdos et al.[15]	1977	$2\frac{1}{2}$	Euler	Time lag	Transonic fan stage[15]	44:46
Koya and Kotake[16]	1985	3	Euler	Time lag	Turbine stage[16]	52:68
Lewis et al.[17]	1989	$2\frac{1}{2}$	Euler	Time lag	Turbine stage[17]	30:45
Giles[18]	1990	$2\frac{1}{2}$	Euler	Time inclining	Transonic turbine stage[18]	36:61
——	1992	2	ML[19],[a]	——	Transonic turbine stage[20]	36:61
Hah et al.[21]	1993	3	k–ε	Time lag	Compressor stage[21]	20:31
——	——	——	——	——	Turbine stage[22]	36:41
Jung et al.[23]	1996	3	ML	Time inclining	Turbine stage[23]	44:60
——	——	——	——	——	Transonic compressor stage[24]	57:58
——	——	——	——	——	$1\frac{1}{2}$-stage turbine[24,25]	36:41:36
——	——	——	——	——	Turbine stage[26]	78:80
Volmar et al.[27]	2000	3	k–ε	Time lag	$1\frac{1}{2}$-stage turbine[27,28]	36:41:36
Present paper	2001	3	[b]RSM	Time lag	$1\frac{1}{2}$-stage turbine[c]	36:41:36
——	——	——	——	——	Transonic compressor IGV/rotor[c]	42:50
——	——	——	——	——	Compressor stage[d]	30:40

[a]ML = mixing length.
[b]RSM Reynolds-stress model.
[c]Present paper.
[d]Presented in "Experimental and Computational Investigation of this Unsteady Aerodynamics of a Compressor Stage at Off-Design Conditions" by G. A. Gerolymos, G. J. Michon, and H. Miton, in preparation.

developed, and the matching conditions for the chorochronic harmonics on each side are established. Then this method is implemented in a three-dimensional Favre–Reynolds-averaged Navier–Stokes solver. The updating of the harmonics is based on a moving-averages technique. The same technique is used for the $t\theta$ harmonics at the interface, and it is shown that these harmonics can be computed by the data in a single blade passage. These harmonics updating techniques, developed in the present work, are computationally efficient and require minimum storage. Then the method is applied to the computation of a $1\frac{1}{2}$-stage turbine[25,38] and compared wirh measurements. Finally, results are also shown for a transonic axial compressor stage, illustrating the ability of the interface treatment to transmit shock waves.

Chorochronic Periodicity

Blade-Row Interaction

Consider (Fig. 1) two blade rows, $n_{\mathrm{BR}} = 1$ and 2, with arbitrary blade numbers N_{B_1} and N_{B_2} (and arbitrary blade number ratio) that are in relative angular motion ($\Omega_1 \neq \Omega_2$). If aerodynamic instabilities are neglected, the unsteady flow in the frame of reference rotating with a given row is periodic with the fundamental frequency of the BPF of the blades of the adjacent blade row

$$f_1 = \left(N_{B_2}/2\pi\right)|\Omega_1 - \Omega_2|, \qquad f_2 = \left(N_{B_1}/2\pi\right)|\Omega_1 - \Omega_2| \quad (1)$$

When considering the flow around two neighboring blades of a given blade row (Fig. 1), each blade witnesses the same phenomena as its neighbor, but with a phase shift β_r in $2\pi f t$ (circumferentially traveling wave). This phase shift is a simple function of the numbers of blades N_{B_1} and N_{B_2} and of the direction of relative rotation ($\mathrm{sign}[\Omega_1 - \Omega_2]$). A uniformly valid expression is[29,39]

$$\beta_{r_1} = -2\pi \frac{N_{B_1} - N_{B_2}}{N_{B_1}} \mathrm{sign}[\Omega_1 - \Omega_2]$$

$$\beta_{r_2} = -2\pi \frac{N_{B_2} - N_{B_1}}{N_{B_2}} \mathrm{sign}[\Omega_2 - \Omega_1] \quad (2)$$

These periodicities indicate that $\boldsymbol{w}$ (in an $[x, R, \theta]$ cylindrical coordinates system with x the engine axis) is invariable through a space–time transformation in each frame of reference

$$\boldsymbol{w}_1(t, \theta_1; x, R) = \boldsymbol{w}_1\left(t + \beta_{r_1}/2\pi f_1, \theta_1 - 2\pi/N_{B_1}; x, R\right)$$

$$\boldsymbol{w}_2(t, \theta_2; x, R) = \boldsymbol{w}_2\left(t + \beta_{r_2}/2\pi f_2, \theta_2 - 2\pi/N_{B_2}; x, R\right) \quad (3)$$

Alternatively (Fig. 1), if $\boldsymbol{F}(2\pi f t)$ is the periodic time signal (measured or computed) for $\boldsymbol{w}(t, \theta; x, R)$, then the time signal for the next blade toward the positive θ direction is

$$\boldsymbol{w}_1(t, \theta_1; x, R) = \boldsymbol{F}_1(2\pi f_1 t)$$

$$\Rightarrow \boldsymbol{w}_1\left(t, \theta_1 + 2\pi/N_{B_1}; x, R\right) = \boldsymbol{F}_1\left(2\pi f_1 t + \beta_{r_1}\right)$$

$$\boldsymbol{w}_2(t, \theta_2; x, R) = \boldsymbol{F}_2(2\pi f_2 t)$$

$$\Rightarrow \boldsymbol{w}_2\left(t, \theta_2 + 2\pi/N_{B_2}; x, R\right) = \boldsymbol{F}_2\left(2\pi f_2 t + \beta_{r_2}\right) \quad (4)$$

Incidentally, it is exactly this traveling wave transformation that is used in the inclined-plane method.[37] With the present sign conventions [Fig. 1 and Eqs. (2–4)], for positive β_r, the wave is traveling in the negative θ direction. (It is coming from the positive θ direction.)

Chorochronic Interface

In a standard numerical treatment of the blade-row interaction problem, two frames of reference are used, one rotating with blade row $n_{\mathrm{BR}} = 1$ and another rotating with blade row $n_{\mathrm{BR}} = 2$ (Fig. 1). At the interface between the two frames of reference, the same phenomena are observed in each frame of reference: 1) Each frame of reference observes a time-periodic signal, but with different frequencies (Doppler shift due to the relative rotation and to the difference in number of blades). 2) The appropriate β_r shift is observed in each frame (β_{r_1}, β_{r_2}). 3) The same signal is observed in each frame as well as in the absolute frame of reference:

$$\boldsymbol{w}(t, \theta_{\mathrm{abs}}; x, R) \equiv \boldsymbol{w}_1(t, \theta_1; x, R) \equiv \boldsymbol{w}_2(t, \theta_2; x, R)$$

$$\theta_{\mathrm{abs}} = \theta_1 + \Omega_1 t = \theta_2 + \Omega_2 t \quad (5)$$

Because of the double periodicity in t and azimuthal coordinate θ (chorochronic periodicity), it is natural to express the signal in each frame of reference by double $t\theta$ Fourier series

$$\boldsymbol{w}_1(t, \theta_1; x, R) = \sum_{n_{t_1}=-\infty}^{+\infty} \sum_{n_{\theta_1}=-\infty}^{+\infty} \hat{\boldsymbol{w}}_1\left(n_{t_1}, n_{\theta_1}; x, R\right) \times \exp\left(i 2\pi n_{t_1} f_1 t + i n_{\theta_1} \theta_1\right)$$

$$\boldsymbol{w}_2(t, \theta_2; x, R) = \sum_{n_{t_2}=-\infty}^{+\infty} \sum_{n_{\theta_2}=-\infty}^{+\infty} \hat{\boldsymbol{w}}_2\left(n_{t_2}, n_{\theta_2}; x, R\right) \times \exp\left(i 2\pi n_{t_2} f_2 t + i n_{\theta_2} \theta_2\right) \quad (6)$$

The phase-lag periodicity [Eqs. (3) and (4)] implies that only a few of the $t\theta$ harmonics can be nonzero. By the use of the Fourier-series expression [Eqs. (6)] of the signals in the expression of the phase-lag periodicity [Eqs. (3)], the reexpression of the difference of the right-hand side (RHS) and the left-hand side (LHS) as a double Fourier series, and the equation of the harmonics coefficients to zero, the nonzero $t\theta$ harmonics can be identified[39]

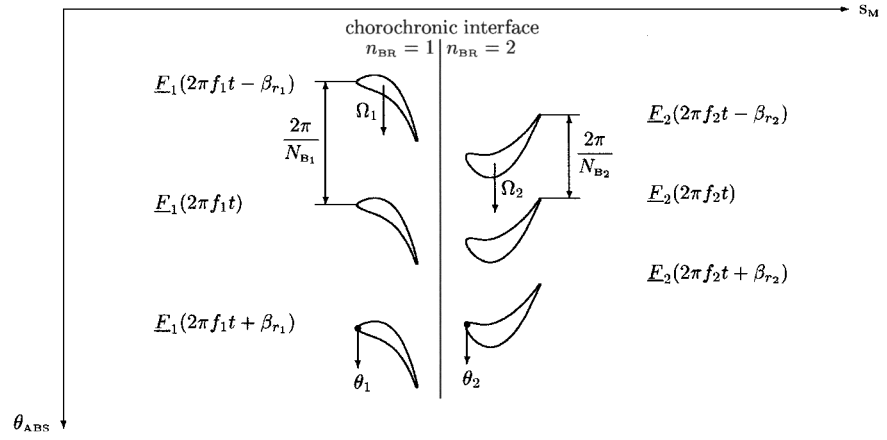

Fig. 1 Chorochronic periodicity of the interaction of two blade rows in relative angular motion ($\Omega_1 \neq \Omega_2$).

$$\boldsymbol{w}(t,\theta_1)=\boldsymbol{w}\left(t+\beta_{r_1}\Big/2\pi f_1,\theta_1-2\pi\Big/N_{B_1}\right)$$
$$\Rightarrow\ n_{\theta_1}\left(n_{t_1},\ell_{\theta_1}\right)=\ell_{\theta_1}N_{B_1}-n_{t_1}\left(N_{B_1}-N_{B_2}\right)$$
$$\times\ \mathrm{sign}[\Omega_1-\Omega_2]\,\ell_{\theta_1}\in\mathbb{Z}$$
$$\boldsymbol{w}(t,\theta_2)=\boldsymbol{w}\left(t+\beta_{r_2}\Big/2\pi f_2,\theta_2-2\pi\Big/N_{B_2}\right)$$
$$\Rightarrow\ n_{\theta_2}\left(n_{t_2},\ell_{\theta_2}\right)=\ell_{\theta_2}N_{B_2}-n_{t_2}\left(N_{B_1}-N_{B_2}\right)$$
$$\times\ \mathrm{sign}[\Omega_1-\Omega_2]\,\ell_{\theta_2}\in\mathbb{Z}\qquad(7)$$

The nonzero harmonics generated by $[n_t,\ell_\theta]$ [Eqs. (7)] correspond to the well known in turbomachinery aeroacoustics Tyler–Sofrin lobe modes.[14] All other harmonics that do not satisfy these relations [Eqs. (7)], that is, harmonics $[n_t,n_\theta]$ for which $\nexists\,\ell_\theta\in\mathbb{Z}$, satisfying the relation [Eqs. (7)] between n_t, n_θ, N_{B_1}, N_{B_2}, and $\mathrm{sign}[\Omega_1-\Omega_2]$, are identically 0. Finally, signals expressed in each frame of reference at the same meridional location (x,R) should match [Eqs. (5)]. By expression of this equality in Fourier series [Eqs. (6)] and the use of the phase-shift conditions [Eqs. (7)], it is easy to show[39] that corresponding chorochronic harmonics in the various frames of reference have the same $n_\theta\equiv n_{\theta_1}\equiv n_{\theta_2}$, but different n_t (due to the Doppler-shift)

$$\hat{\boldsymbol{w}}_1\left(n_{t_1},n_\theta;x,R\right)\equiv\hat{\boldsymbol{w}}_2\left(n_{t_2},n_\theta;x,R\right)$$
$$n_{t_1}-n_{t_2}=\ell_\theta\,\mathrm{sign}[\Omega_1-\Omega_2],\qquad\ell_\theta\in\mathbb{Z}$$
$$n_\theta=n_{\theta_1}\left(n_{t_1},\ell_\theta\right)=n_{\theta_2}\left(n_{t_2},\ell_\theta\right)=\ell_\theta N_{B_1}-n_{t_1}\left(N_{B_1}-N_{B_2}\right)$$
$$\times\ \mathrm{sign}[\Omega_1-\Omega_2]=\ell_\theta N_{B_2}-n_{t_2}\left(N_{B_1}-N_{B_2}\right)\mathrm{sign}[\Omega_1-\Omega_2]\qquad(8)$$

where the same $\ell_\theta=\ell_{\theta_1}=\ell_{\theta_2}$ should be used in the relations for corresponding harmonics. The meaning of corresponding harmonics is that they are the same harmonics of the signal as viewed in the two reference frames. These relations [Eqs. (8)] are the most important result of the present work, because they allow a mathematically simple representation of the interface and include the fundamental matching conditions[39] (for $N_{B_1}\neq N_{B_2}$ and $\Omega_1\neq\Omega_2$): The meridional average ($\ell_\theta=0$) is

$$\hat{\boldsymbol{w}}_1(0,0;x,R)=\hat{\boldsymbol{w}}_2(0,0;x,R)\qquad(9a)$$

The $|n_\theta|=N_{B_1}$ harmonic ($\ell_\theta=\pm1$) is

$$\hat{\boldsymbol{w}}_1\left(0,\pm N_{B_1};x,R\right)=\hat{\boldsymbol{w}}_2\left(\mp\mathrm{sign}[\Omega_1-\Omega_2],\pm N_{B_1};x,R\right)\qquad(9b)$$

The $|n_\theta|=N_{B_2}$ harmonic ($\ell_\theta=\pm1$) is

$$\hat{\boldsymbol{w}}_1\left(\pm\mathrm{sign}[\Omega_1-\Omega_2],\pm N_{B_2};x,R\right)=\hat{\boldsymbol{w}}_2\left(0,\pm N_{B_2};x,R\right)\qquad(9c)$$

The $|n_\theta|=|N_{B_1}-N_{B_2}|$ harmonic ($\ell_\theta=0$) is

$$\hat{\boldsymbol{w}}_1\left(\mp\mathrm{sign}[\Omega_1-\Omega_2],\pm\left[N_{B_1}-N_{B_2}\right];x,R\right)$$
$$=\hat{\boldsymbol{w}}_2\left(\mp\mathrm{sign}[\Omega_1-\Omega_2],\pm\left[N_{B_1}-N_{B_2}\right];x,R\right)\qquad(9d)$$

The $|n_\theta|=N_{B_1}+N_{B_2}$ harmonic ($\ell_\theta=\pm2$) is

$$\hat{\boldsymbol{w}}_1\left(\pm\mathrm{sign}[\Omega_1-\Omega_2],\pm\left[N_{B_1}+N_{B_2}\right];x,R\right)$$
$$=\hat{\boldsymbol{w}}_2\left(\mp\mathrm{sign}[\Omega_1-\Omega_2],\pm\left[N_{B_1}+N_{B_2}\right];x,R\right)\qquad(9e)$$

Furthermore, when chorochronic periodicity is valid, the interface signals can be expressed as a series of n_t and ℓ_θ,

$$\boldsymbol{w}_1(t,\theta_1;x,R)=\sum_{n_{t_1}=-\infty}^{+\infty}\sum_{l_{\theta_1}=-\infty}^{+\infty}\hat{\boldsymbol{w}}_1\left(n_{t_1},n_{\theta_1};x,R\right)$$
$$\times\exp\left(i2\pi n_{t_1}f_1t+in_{\theta_1}\theta_1\right)$$
$$n_{\theta_1}=n_{\theta_1}\left[n_{t_1},\ell_\theta\right]=[\text{Eqs. (8)}]$$
$$\boldsymbol{w}_2(t,\theta_2;x,R)=\sum_{n_{t_2}=-\infty}^{+\infty}\sum_{l_{\theta_2}=-\infty}^{+\infty}\hat{\boldsymbol{w}}_2\left(n_{t_2},n_{\theta_2};x,R\right)$$
$$\times\exp\left(i2\pi n_{t_2}f_2t+in_{\theta_2}\theta_2\right)$$
$$n_{\theta_2}=n_{\theta_2}\left[n_{t_2},\ell_\theta\right]=[\text{Eqs. (8)}]\qquad(10)$$

where only the nonzero chorochronic harmonics appear.

Single Blade Modeling

These periodicities can be applied to compute the aerodynamic interaction between two blade rows in relative rotation, discretizing the flow around only one blade per blade row.[15–27] This results in substantial computational economy, without any restriction in blade number ratio (N_{B_2}:N_{B_1}). In the present implementation, phantom nodes are used for both the pitchwise boundaries (Fig. 2) and for the blade-row interface (Fig. 3). The pitchwise phantom nodes are geometrically the same as those used for steady computations by Gerolymos et al.[40] The interface phantom nodes are geometrically the same as those used for steady multistage mixing-plane computations by Gerolymos and Hanisch.[41] (Phantom node P' in Fig. 3 at the downstream chorochronic interface of blade row $n_{\mathrm{BR}}=1$ does not correspond to any existing node, but the flowfield values at each iteration are reconstructed by computing chorochronic harmonics using a moving-average technique requiring only instantaneous values in the sector $Q_-\ Q_+$ of blade row $N_{\mathrm{BR}}=2$). The methodology can, of course, be applied to solvers that do not employ phantom nodes for the treatment of boundaries between adjacent grid domains.

Pitchwise Boundaries

The phantom nodes at the pitchwise boundaries (Fig. 2) are updated using the corresponding nodes of the computational domain at $\theta\pm2\pi/N_B$. For this purpose, the time signals at each phantom-generating node P (Fig. 2) are stored as time Fourier series,

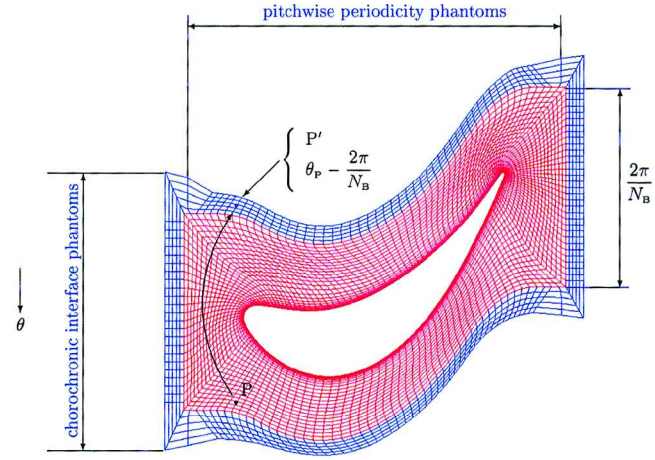

Fig. 2 Typical grid around the blade (red nodes) and phantom nodes[40] (blue); point P generates a phantom (P') pitchwise periodicity node, updated using phase-lag relations [Eq. (12)].

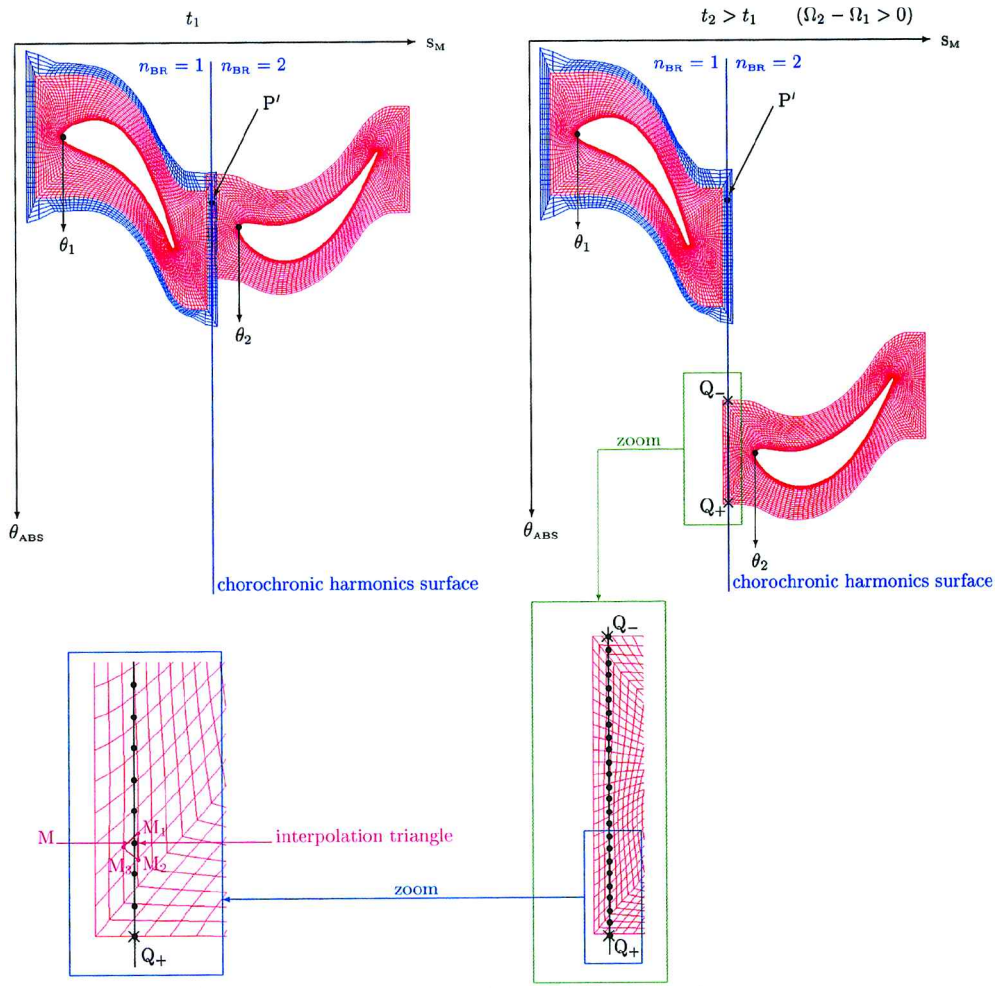

Fig. 3 Typical grid around the blades of two adjacent blade rows $n_{BR} = 1, 2$ (red nodes) and phantom nodes of blade row $n_{BR} = 1$ (blue nodes) for two different instants t_1 and t_2.

truncated at N_t. For any blade row, in the frame of reference rotating with it

$$\boldsymbol{w}(t; x, R, \theta) = \Re\left\{\sum_{n_t=0}^{+\infty} \check{\boldsymbol{w}}(n_t; x, R, \theta)\exp(i2\pi n_t f t)\right\}$$

$$\cong \Re\left\{\sum_{n_t=0}^{+N_t} \check{\boldsymbol{w}}(n_t; x, R, \theta)\exp(i2\pi n_t f t)\right\} \qquad (11)$$

where the symbol $\check{\boldsymbol{w}}$ is used to distinguish time harmonics from chorochronic harmonics $\hat{\boldsymbol{w}}$. Fourier series with only $n_t \geq 0$ harmonics are used for the time series because this diminishes storage by a factor of two. The phase-lagged chorochronic periodicity conditions [Eqs. (4)] are used in updating the phantom nodes (more precisely, the time harmonics of the phantom nodes),

$$\check{\boldsymbol{w}}(n_t; x, R, \theta \pm 2\pi/N_B) = \check{\boldsymbol{w}}(n_t; x, R, \theta)e^{\pm i n_t \beta_r} \qquad (12)$$

Equations (11) and (12) apply to blade row $n_{BR} = 1$ (respectively, 2) by using n_{t_1}, θ_1, f_1, and β_{r_1} (respectively, n_{t_2}, θ_2, f_2, and β_{r_2}). The numerical implementation requires computing the harmonics at only the phantom-generating nodes. It is not necessary to store the time signal. Instead, a moving-averages technique that updates the harmonics is used (see Appendix). Typically, $N_t = \mathcal{O}(10)$ harmonics are sufficient to give a satisfactory representation of the time signals.

Blade-Row Interface

The blade-row interface is also treated using phantom nodes (Fig. 3) and a chorochronic harmonics technique [Eqs. (10)]. These phantom nodes are located at N_{PH} (for the computations reported in the present paper, $N_{PH} = 5$) surfaces of revolution (Fig. 2) (Ref. 41). In the following, the treatment of the downstream interface of blade row $n_{BR} = 1$ (Fig. 3) is examined. (The upstream interface of blade row $n_{BR} = 2$ is treated in an exactly analogous way.) The use of several (N_{PH}) streamwise phantoms at the interfaces offers the possibility of matching not only the flowfield, but also its streamwise gradients at the interface. This technique allows the treatment of large regions of separated flow at the interface (within the hub and casing boundary layers), as was demonstrated by steady flow multistage computations using a mixing-plane technique with an exactly analogous phantom nodes implementation.[41]

Consider a phantom node P' at the downstream interface of blade row $n_{BR} = 1$ (Fig. 3). This phantom node P' does not correspond to an existing node of the adjacent blade row ($n_{BR} = 2$) grid. This grid is displaced due to the relative rotation ($\Omega_1 - \Omega_2 \neq 0$) of the two blade rows. (Note that the flow around only one blade per blade row is simulated.) Flowfield variables at phantom nodes, such as P', must be updated at every iteration using information from real (nonphantom) grid points. To do this, the chorochronic harmonics [Eqs. (10)] at the circle $\theta \in [0, 2\pi]$, passing through the point P' (Fig. 3), are used. If these harmonics are known in the frame of reference of the adjacent blade row $n_{BR} = 2$, then it is straightforward to compute the flowfield at the phantom node P' [Eqs. (5) and (10)], using Fourier series truncated to N_t (time) and to L_θ (space)

$$\boldsymbol{w}_1\left(t, \theta_{1_{P'}}; x_{P'}, R_{P'}\right) \equiv \boldsymbol{w}_2\left(t, \theta_{2_{P'}}; x_{P'}, R_{P'}\right) \cong \sum_{n_{t_2}=-N_t}^{+N_t} \sum_{l_\theta=-L_\theta}^{+L_\theta}$$

$$\times\, \hat{\boldsymbol{w}}_2\left(n_{t_2}, n_{\theta_2}; x_{P'}, R_{P'}\right)\exp\left(i2\pi n_{t_2} f_2 t + i n_{\theta_2}\theta_{2_{P'}}\right) \qquad (13)$$

where $\theta_{2_{P'}} = \theta_{\text{abs}_{P'}} - \Omega_2 t = \theta_{1_{P'}} + (\Omega_1 - \Omega_2)t$ [Eqs. (5)], and $n_{\theta_2} = n_{\theta_2}[n_{t_2}, \ell_\theta]$ [Eqs. (8)].

The underlying idea is to compute the chorochronic harmonics at point P' (phantom node of blade row $n_{\text{BR}} = 1$) using values at the nodes of the grid of the adjacent blade row $n_{\text{BR}} = 2$. The circle (chorochronic harmonics surface) passing through point P' (more precisely, through point $[x_{P'}, R_{P'}]$ of the meridional plane) intersects the contour of the grid of blade row $n_{\text{BR}} = 2$ at points Q_- and Q_+ (Fig. 3), so that at every iteration, information for computing the chorochronic harmonics is available in the sector $Q_-Q_+(\theta_{Q_+} - \theta_{Q_-} = 2\pi N_{B_2}^{-1})$. Auxiliary points M, noted as full black dots (Fig. 3), are used to discretize this sector ($[x_M, R_M] = [x_{P'}, R_{P'}]$), and the instantaneous values of the flowfield variables at each point M are computed using area interpolation[42] in the triangle $M_1M_2M_3$ of surrounding nodes of the blade row $n_{\text{BR}} = 2$ grid (Fig. 3). The number of auxiliary points M is taken equal to the number of blade row $n_{\text{BR}} = 2$ grid nodes at the interface (points M are equidistant θ-wise). The values at points M are used in conjuction with a moving-averages technique (described in the Appendix) to compute the required chorochronic harmonics $\hat{\boldsymbol{w}}_2(n_{t_2}, n_{\theta_2}; x_{P'}, R_{P'})$, which are used to determine the flowfield at point P' [Eq. (13)].

Flow Model and Numerics

The technique just described is generic and can be used with various flow models. In the present work, the flow is modeled using the Favre–Reynolds-averagedNavier–Stokes equations with a wall-normal-free near-wall Reynolds-stress turbulence closure. The flow model and turbulence closure are described in detail by Gerolymos and Vallet,[43,44] and steady flow turbomachinery validations have been reported in Gerolymos et al.[45] The flow is described by 12 variables (five mean flow variables $\boldsymbol{v}_{\text{MF}} \in \mathbb{R}^5$ and seven turbulence model variables $\boldsymbol{v}_T \in \mathbb{R}^7$)

$$\boldsymbol{v} = \left[\boldsymbol{v}_{\text{MF}}^T; \boldsymbol{v}_T^T\right] = \left[\bar{\rho}, \tilde{V}_x, \tilde{V}_R, \tilde{V}_\theta, \bar{p}; \times \widetilde{v_x'' v_x''}, \widetilde{v_x'' v_R''}, \widetilde{v_R'' v_R''}, \widetilde{v_R'' v_\theta''}, \widetilde{v_\theta'' v_\theta''}, \widetilde{v_\theta'' v_x''}, \varepsilon^*\right]^T \in \mathbb{R}^{12} \tag{14}$$

where (V_x, V_R, V_θ) are the absolute velocity components, $(v_x'', v_R'', v_\theta'')$ are the velocity fluctuations, ε^* is the modified turbulence dissipation rate, the overbar indicates nonweighted averaging, and the prime indicates nonweighted fluctuations.[43] To ensure massflow conservation at the interfaces, time harmonics and chorochronic harmonics are computed for the vector

$$\boldsymbol{u} = \left[\boldsymbol{u}_{\text{MF}}^T; \boldsymbol{u}_T^T\right] = \left[\bar{\rho}, \bar{\rho}\tilde{V}_x, \bar{\rho}\tilde{V}_R, \bar{\rho}\tilde{V}_\theta, \bar{p}; \widetilde{v_x'' v_x''}, \times \widetilde{v_x'' v_R''}, \widetilde{v_R'' v_R''}, \widetilde{v_R'' v_\theta''}, \widetilde{v_\theta'' v_\theta''}, \widetilde{v_\theta'' v_x''}, \varepsilon^*\right]^T \in \mathbb{R}^{12} \tag{15}$$

The corresponding 12 transport equations are written using a conservative Cartesian (x, y, z) formulation,[44,45] in the relative frame of reference of each blade row

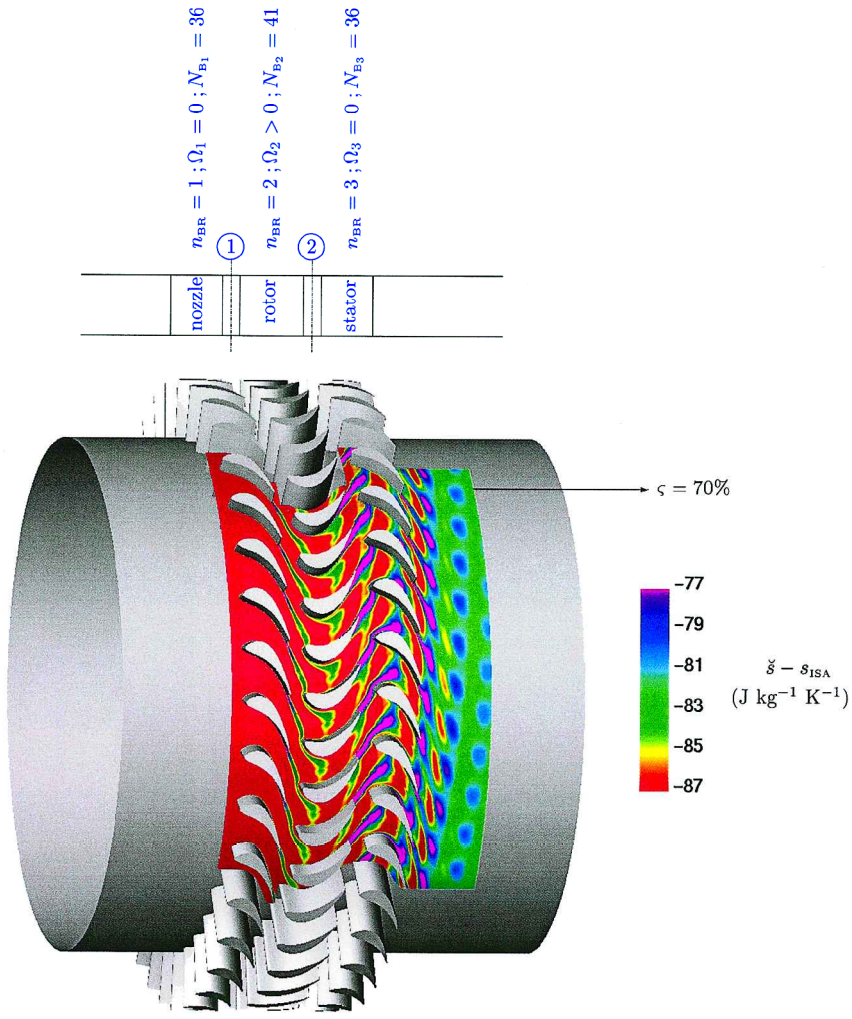

Fig. 4 Computed instantaneous entropy contours ($\check{s} - s_{\text{ISA}}$, where s_{ISA} is the entropy at standard total conditions[47] $pt_{\text{ISA}} = 101{,}325$ Pa and $Tt_{\text{ISA}} = 288.15$ K) at 70% span of the RWTH_1 turbine. (Note that due to the 36:41:36 blade numbers ratio, there is no instantaneous space periodicity other then the full circumference.)

$$\boldsymbol{c} = \left[\boldsymbol{c}_{\mathrm{MF}}^T; \boldsymbol{c}_T^T\right] = \left[\bar{\rho}, \bar{\rho}\breve{W}_x, \bar{\rho}\breve{W}_y, \bar{\rho}\breve{W}_z, \bar{\rho}\breve{H}_{\mathrm{R}} - \bar{p}; \bar{\rho}\widetilde{w''_x w''_x}, \bar{\rho}\widetilde{w''_x w''_y}, \times \bar{\rho}\widetilde{w''_y w''_y}, \bar{\rho}\widetilde{w''_y w''_z}, \bar{\rho}\widetilde{w''_z w''_z}, \bar{\rho}\widetilde{w''_z w''_x}, \bar{\rho}\varepsilon^*\right]^T \in \mathbb{R}^{12} \quad (16)$$

where (W_x, W_y, W_z) are the relative velocity components, (w''_x, w''_y, w''_z) the corresponding velocity fluctuations, and $H_R = \tilde{h} + \frac{1}{2}W^2 - \frac{1}{2}\Omega^2 R^2$ the rothalpy of the mean flow.[44] These equations are discretized on a structured grid generated biharmonically.[46] A multidomain strategy is used for the discretization of tip clearance,[40,47] and a multiblock strategy is used for multistage configurations.[41] The mean flow and turbulent variables are discretized in space using an $\mathcal{O}(\Delta x^3)$ upwind MUSCL scheme with van Leer flux-vector splitting and van Albada limiters.[48,49] An $\mathcal{O}(\Delta t^2)$ dual time-stepping implicit time-integration technique is used in the present unsteady computations.[49] At the solid surfaces, no-slip boundary conditions are used, whereas nonreflecting $2\frac{1}{2}$-dimensional boundary conditions are used at the inflow and outflow boundaries, as noted in "Boundary Conditions for Three-Dimensional Steady and Unsteady Turbomachinery Computations," currently being written by J. C. Chassaing and G. A. Gerolymos. The nonreflecting boundary conditions do not concern the meridional averages ($[n_t, n_\theta] = [0, 0]$), for which standard reservoir-inflow and throttle-outflow boundary conditions were used.[40]

Results and Comparison with Measurements

Configurations Studied

The validity of the methodology is illustrated by computing two configurations: 1) a subsonic $1\frac{1}{2}$-stage axial flow turbine, where the nozzle and the stator have the same number of blades so that chorochronic periodicity conditions apply and 2) the interaction between a transonic compressor rotor and its inlet guide vane (IGV), illustrating the ability of the interface treatment to correctly transmit shock waves.

Further computations and comparisons with measurements for a high-subsonic compressor stage are reported by G. A. Gerolymos, G. J. Michon, and H. Miton in "Experimental and Computational Investigation of the Unsteady Aerodynamics of a Compressor Stage at Off-Design Conditions," currently being written. Unsteady computations are initialized from converged steady computations based on a mixing-plane approach.[41]

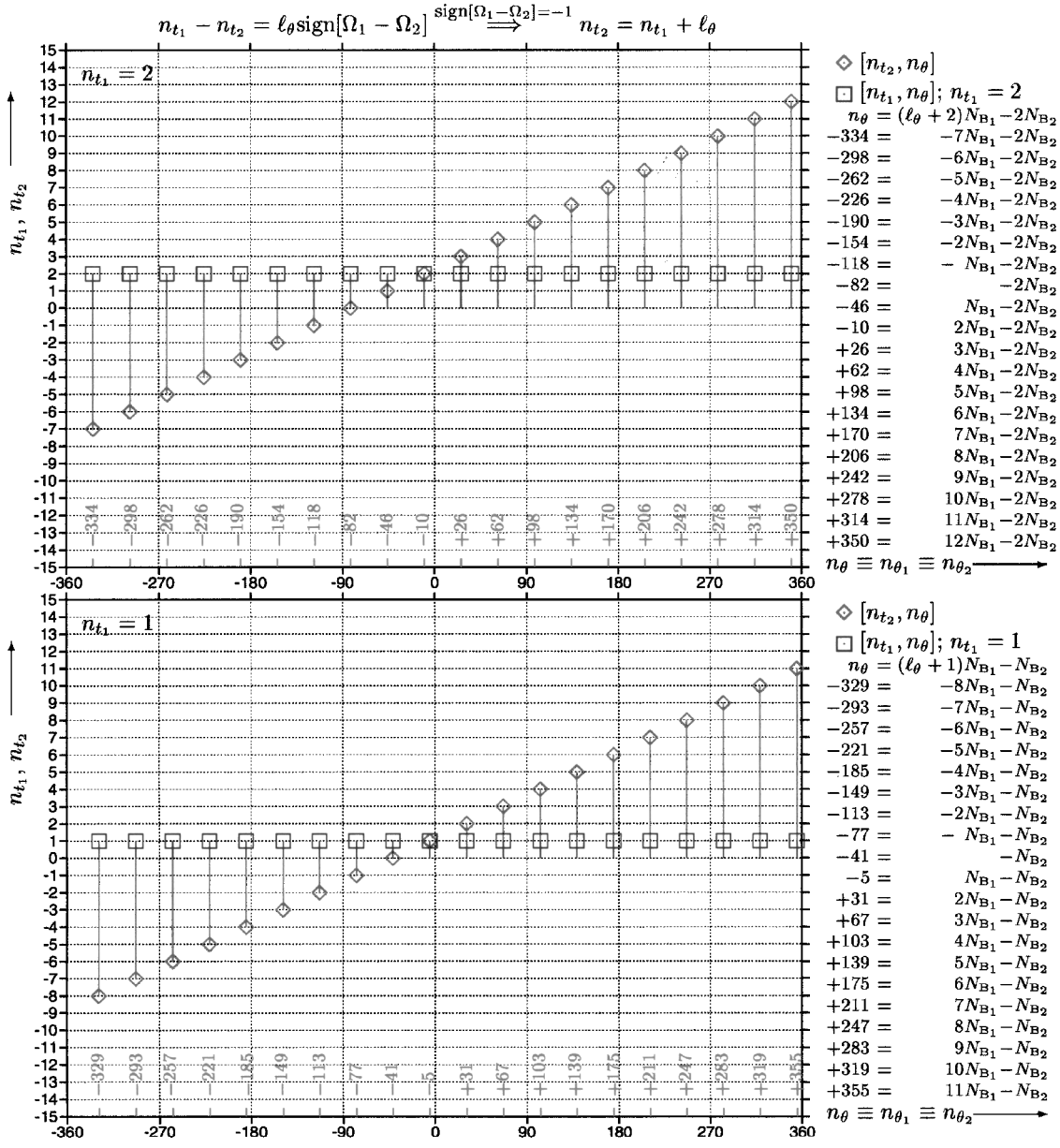

Fig. 5 Chorochronic harmonics correspondance on each side of the nozzle/rotor interface (plane 1, Fig. 4) of the RWTH $1\frac{1}{2}$-stage turbine[28,38] ($\mathrm{sign}[\Omega_1 - \Omega_2] = -1$, $N_{B_1} = 36$, and $N_{B_2} = 41$).

Turbine $1\frac{1}{2}$-Stage

Computations were run for a $1\frac{1}{2}$-stage axial flow turbine (Fig. 4), investigated at the Institut für Strahlantriebe und Turboarbeitsmaschinen of the RWTH, both experimentally[28,38] and computationally.[22,25] Because for this configuration (Fig. 4) the nozzle and the stator have the same number of blades ($N_{B_1} = N_{B_3} = 36$) chorochronic periodicity conditions are applicable for the entire $1\frac{1}{2}$-stage. This has been exploited in computational work by Gallus et al.,[22] Walraevens et al.,[25] Volmar et al.,[27] and Reinmoeller et al.[28] Steady computations using the present turbulence closure and numerical scheme, along with a mixing-plane approach[41] using four different grids (of 1, 2.3, 3, and 4.4×10^6 points), have been compared with measurements in Gerolymos et al.,[45] indicating that the 4.4×10^6 points grid (Table 2) attained grid convergence. This grid, which has 121 radial surfaces and models the tip-clearance gap with 41 radial surfaces (completely independent of the main grid thanks to the use of a buffer domain[42]), was used in the present computations.

The chorochronic interface treatment is illustrated by considering the nozzle/rotor ($[n_{\mathrm{BR}} = 1]/[n_{\mathrm{BR}} = 2]$) interface (plane 1, Fig. 4). At this interface, the chorochronic periodicity relations [Eqs. (8)] are applicable with $\mathrm{sign}[\Omega_1 - \Omega_2] = \mathrm{sign}[0 - \Omega_2] = -1$ because $\Omega_2 > 0$. It is easy to plot the corrresponding chorochronic harmonics $[n_{t_1}, n_\theta] \leftrightarrow [n_{t_2}, n_\theta]$ in each frame of reference in the range $n_\theta \in [-360, 360]$ (Fig. 5). The nozzle frame of reference nonzero chorochronic harmonics corresponding to $n_{t_1} = 1, 2$ are generated [Eqs. (8)] by $n_\theta = (\ell_\theta + n_{t_1})N_{B_1} - n_{t_1}N_{B_2}$ (Fig. 5), and the corresponding Doppler shift in the rotor frame of reference is given by [Eqs. (8)] $n_{t_2} = n_{t_1} + \ell_\theta \ell_\theta \in \mathbb{Z}$ (Fig. 5). Only the positive time harmonics $n_{t_1} = 1, 2$ are plotted because the $t\theta$ harmonics appear in pairs ($[n_t, n_\theta]$ and $[-n_t, -n_\theta]$) with complex conjugate Fourier coefficients ($\hat{\boldsymbol{w}}[-n_t, -n_\theta] = \mathrm{conj}\{\hat{\boldsymbol{w}}[n_t, n_\theta]\}$) because $\boldsymbol{w}[t, \theta]$ is real [Eqs. (6)]. The $n_\theta = \pm 360$ harmonics have a 1-deg θ period and correspond to the θ harmonic number 10 over the nozzle pitch ($N_{B_1} = 36$). It is obvious that, due to the chorochronic periodicity conditions [Eqs. (6) and (7)], only a few chorochronic

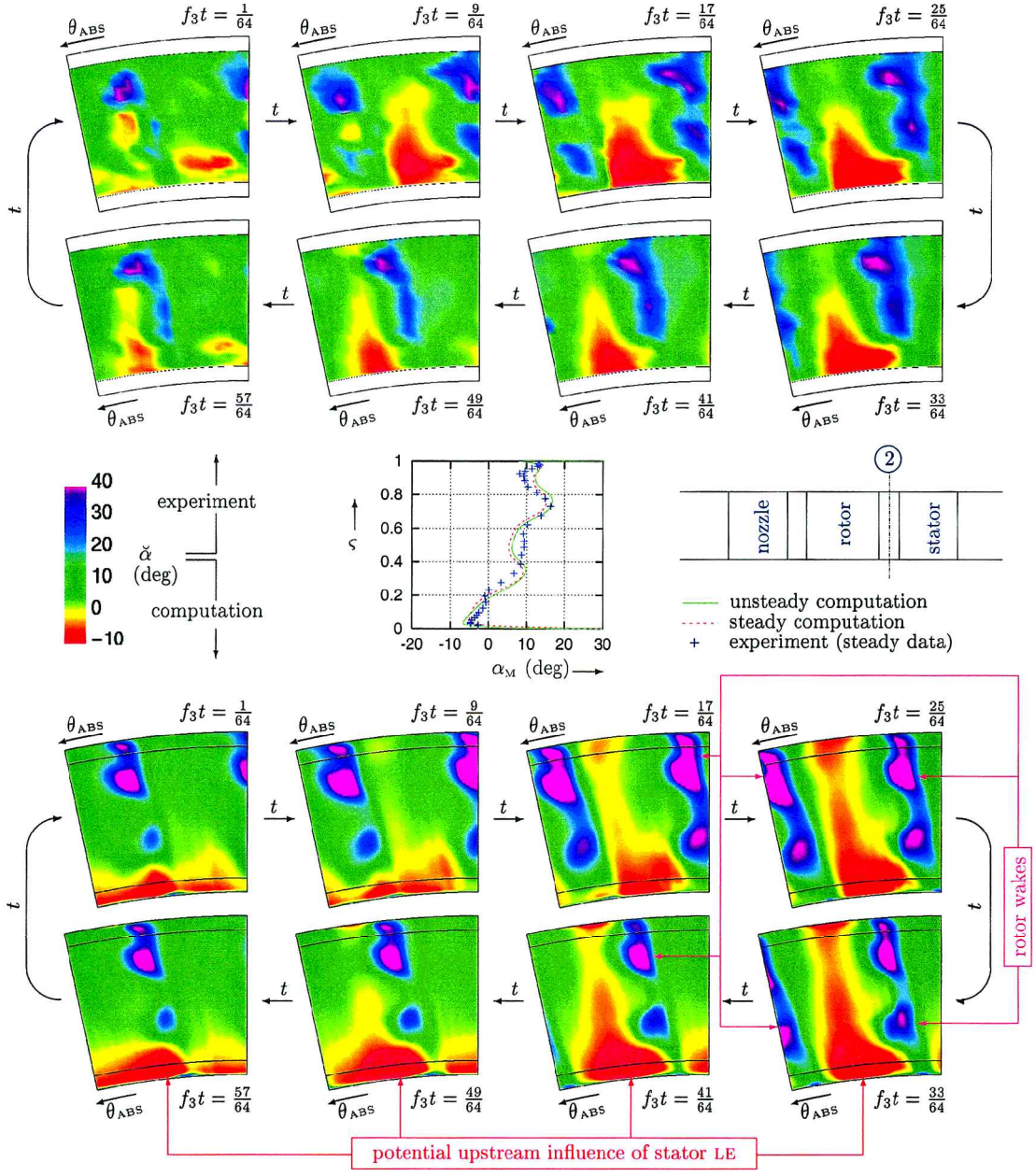

Fig. 6 Computed and measured[39] instantaneous level plots of absolute flow angle $\check{\alpha}$, for various instants of the RTR–BPF ($f_{\mathrm{abs}} = f_1 = f_3$), at rotor-exit (plane 2) of the RWTH $1\frac{1}{2}$-stage turbine[28,38] (rear view, flow coming outward toward the observer), over a sector of 12 deg (nozzle–stator–pitch = 10 deg and RTR–pitch = 8.78 deg) in the absolute frame of reference ($\dot{m} = 8.2$ kg s^{-1} and 3500 rpm).

Table 2 Computational grid summary[40]

Grid	UH[a]	O[b]	DH[c]	TC[d]	OZ[e]	Points[f]	$n^+_{w_B}$ [g]	$n^+_{w_{FP}}$ [h]
			RWTH-1 1½-stage turbine					
D	31 × 31 × 121	201 × 49 × 121	41 × 41 × 121	201 × 31 × 41	201 × 26 × 61	4,359,380	<1.0	<0.7
			Transonic compressor stage					
B	30 × 31 × 65	201 × 53 × 65	50 × 41 × 65	201 × 17 × 25	201 × 21 × 35	1,664,015	<0.5	<1

[a]Upstream H grid (axial × tangential × radial).
[b]O = blades O grid (around the blade × away from blade × radial).
[c]DH = downstream H grid (axial × tangential × radial).
[d]TC = tip-clearance O grid (around the blade × away from blade × radial).
[e]O_Z = O zoom grid (around the blade × away from blade × radial).
[f]Without O-grid points overlapped by the OZ grid.
[g]$n^+_{w_B} = n^+_w$ on the blades.
[h]$n^+_{w_{FP}} = n^+_w$ on the flowpath.

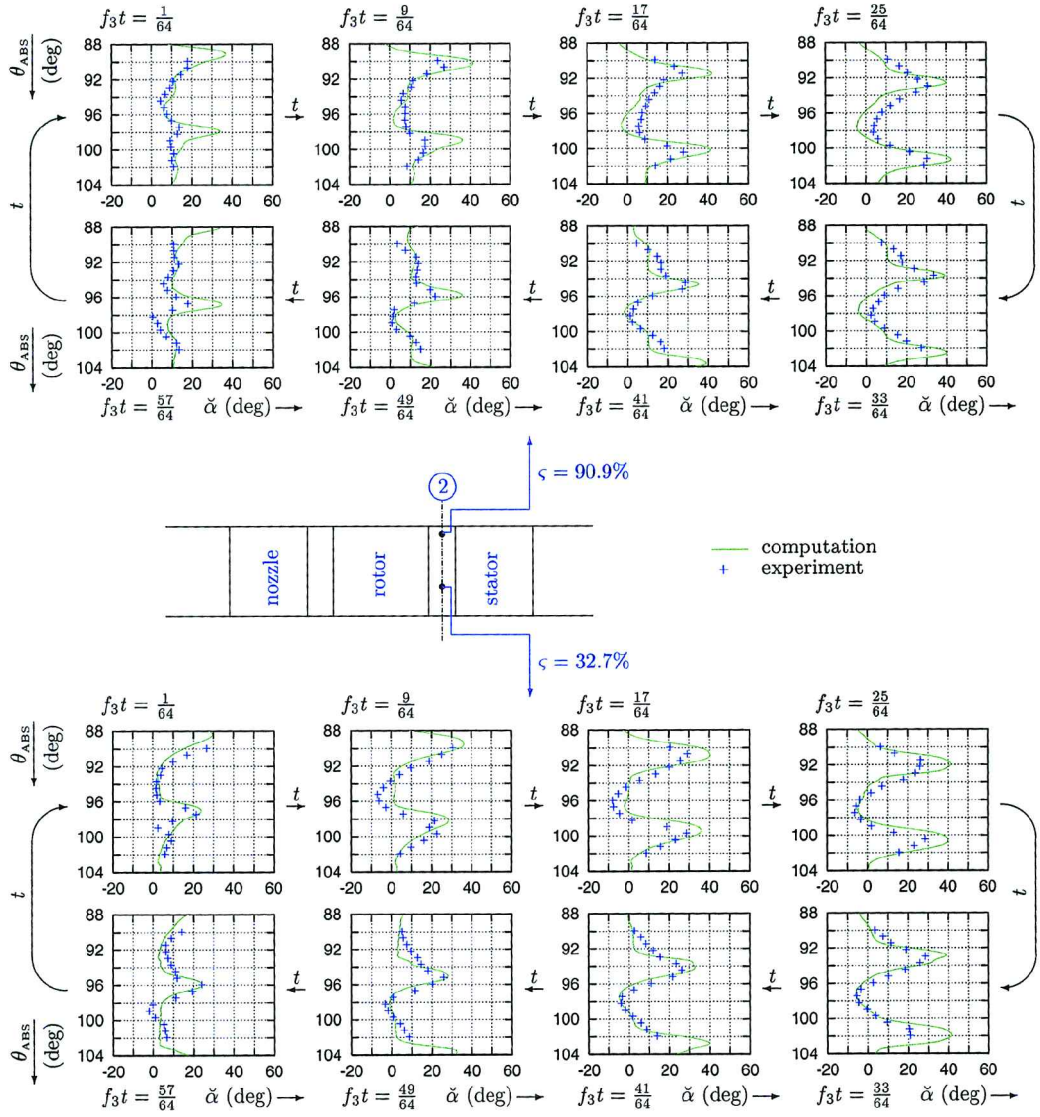

Fig. 7 Comparison of computed and measured[38] instantaneous pitchwise distributions of absolute flow angle $\breve{\alpha}$, at two spanwise locations (ς = 90.9 and 32.7%), for various instants of the RTR–BPF ($f_{abs} = f_1 = f_3$), at RTR exit (plane 2) of the RWTH 1½-stage turbine,[28,38] over a sector of 12 deg (nozzle–stator–pitch = 10 deg and RTR–pitch = 8.78 deg) in the absolute frame of reference ($\dot{m}$ = 8.2 kg s^{-1} and 3500 rpm).

harmonics are nonzero for each n_t, allowing a low-memory treatment of the chorochronic interface. The maximum n_θ-generating index $L_\theta(\ell_\theta \in [-L_\theta, L_\theta])$ can be interpreted as the number of θ harmonics in the pitch of the blade row ($2\pi N_B^{-1}$), so that truncating the Fourier series to $L_\theta = \mathcal{O}(10)$ means that $\mathcal{O}(10)$ θ harmonics over the blade pitch are retained for the fundamental time frequency. Incidentally, it is quite possible to make a fully automatic choice of N_t and L_θ, based on the number of pitchwise grid points at the interface by the use of the well-known sampling theorem.[50]

Computed instantaneous levels of absolute flow angle $\breve{\alpha}$ at the rotor/stator ($[n_{BR} = 2]/[n_{BR} = 3]$) interface (plane 2, Fig. 4) compare quite favorably with measurements, both qualitatively (Fig. 6) and quantitatively (Fig. 7). Both the potential effect of the stator leading edge (nonrotating in the absolute frame of reference) and the rotor wakes (rotating in the absolute frame of reference) are clearly seen in the level plots (Fig. 6). The variation of flow angle is predicted quite well (Fig. 7). The radial distribution of the pitchwise-averaged steady absolute flow angle α_M (obtained with

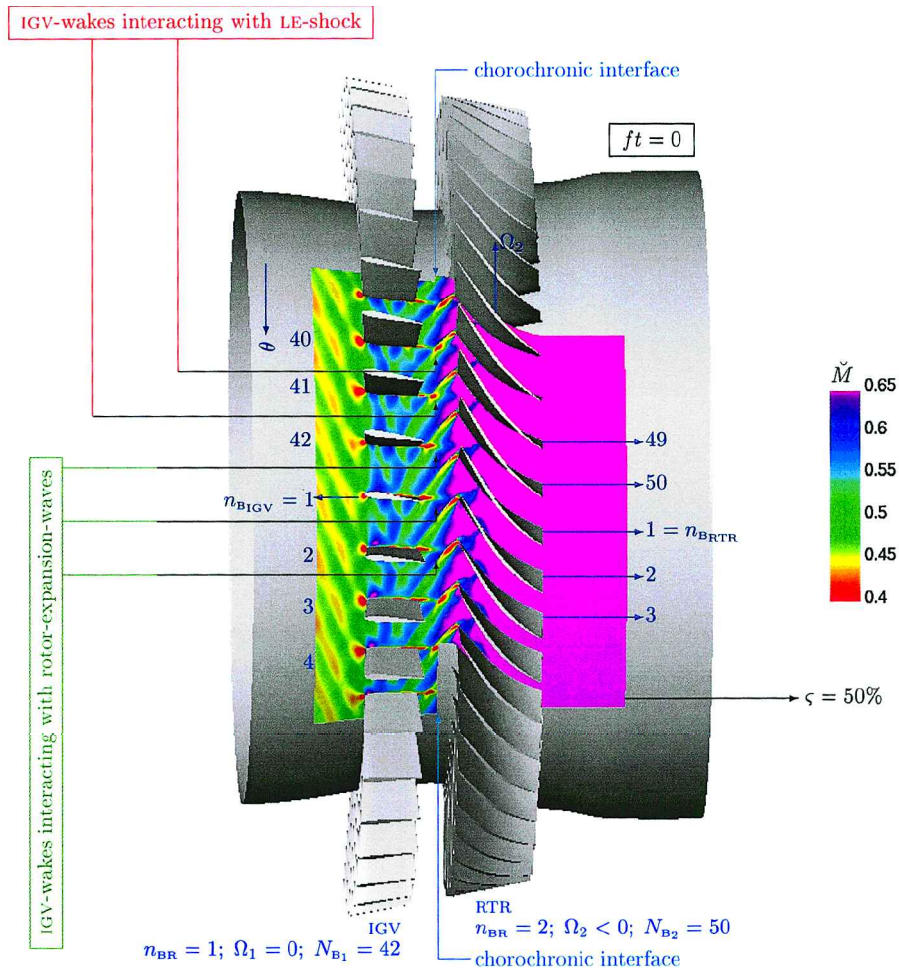

Fig. 8 Instantaneous ($t = 0$) levels of absolute Mach number $\breve{M}$ at midspan of the transonic compressor (design operating point).

the steady mixing-plane multistage computation[45]) compares quite well with the time-averaged result of the present unsteady computations (corresponding to the $[n_{t_3}, n_\theta] = [0, 0]$ chorochronic harmonic) and with the experimental rake measurements (Fig. 6). The unsteady results were taken after the simulation of 15 absolute frame of reference (rotor-BPF) periods, which were sufficient to obtain periodic convergence.

Transonic Compressor Stage

The turbine $1\frac{1}{2}$-stage results just presented illustrate the ability of the chorochronic interface methodology to treat wakes and upstream potential influence in subsonic flow. To demonstrate the validity of the methodology in the presence of shock waves, computations were also run for a transonic compressor rotor (tip relative Mach number at rotor inlet $M_W \sim 1.4$) interacting with its IGV (Fig. 8). Computations were run using a 1.6×10^6 points grid (Table 2) with 65 radial stations. (The rotor tip clearance gap is discretized using 25 radial stations that are completely independent of the 65 radial stations of the blade-to-blade grid.[40]). The unsteady results were taken after the simulation of 15 absolute frame-of-reference (rotor-BPF) periods, which were sufficient to obtain periodic convergence. Plots of instantaneous absolute Mach number at midspan (Fig. 8) clearly show the wave system of the rotor (RTR) leading edge (LE). These waves (LE shock followed by the expansion waves of the suction-side acceleration[51]) interact with the wakes of the IGV, the IGV blades, and then propagate upstream (Fig. 8). Depending on the position of the IGV blade relative to the RTR-LE, the wakes of the IGV interact either with the LE shock or with the expansion waves (Fig. 8).

This explains the pattern of instantaneous absolute Mach number plots at the IGV/RTR interface (Fig. 9). The surface plotted (surface 1, Fig. 9) is the actual computational interface that is treated using the chorochronic harmonics methodology (chorochronic interface, Fig. 8). Because of the blade-numbers ratio ($N_{B_1}:N_{B_2} = 42{:}50 = 21{:}25$) there is a two-lobe (180-deg) θ periodicity of the instantaneous flow pattern (Fig. 9). When the wakes of the IGV interact with the RTR LE shock (e.g., $n_{B_{IGV}} = 35$, 36, 40, and 41) there is a marked low Mach region from hub to tip, marking the wake location (Fig. 9). When the wakes of the IGV interact with the expansion waves of the RTR entry (e.g., $n_{B_{IGV}} = 42$, 1, 2, 6, and 7) the low Mach region is limited to the hub neighborhood.

Table 3 Computing time requirements[a]

Grid	Points[b]	N_{PP}	Simulated periods	CPU
	RWTH_1 $1\frac{1}{2}$-stage turbine			
A[45]	1,010,772	72	16	25
D (Table 2)	4,359,380	144	15	170
	Transonic compressor stage			
B (Table 2)	1,664,015	72	14	59

[a]On an NEC-SX5 computer (average code performance 2.1 Gflops).
[b]Without O-grid points overlapped by the O_Z grid.

Computing Time Requirements

The advantage of chorochronic methodologies is that computations are run discretizing the flow around a single blade per blade row, allowing simulations on fine grids with realistic computing times (Table 3). In practice, the time discretization is defined by choosing the number of instants per period N_{PP}. (The highest of the two frequencies corresponding to each blade row is used to define the period.) In the dual time-stepping technique used,[49] the error

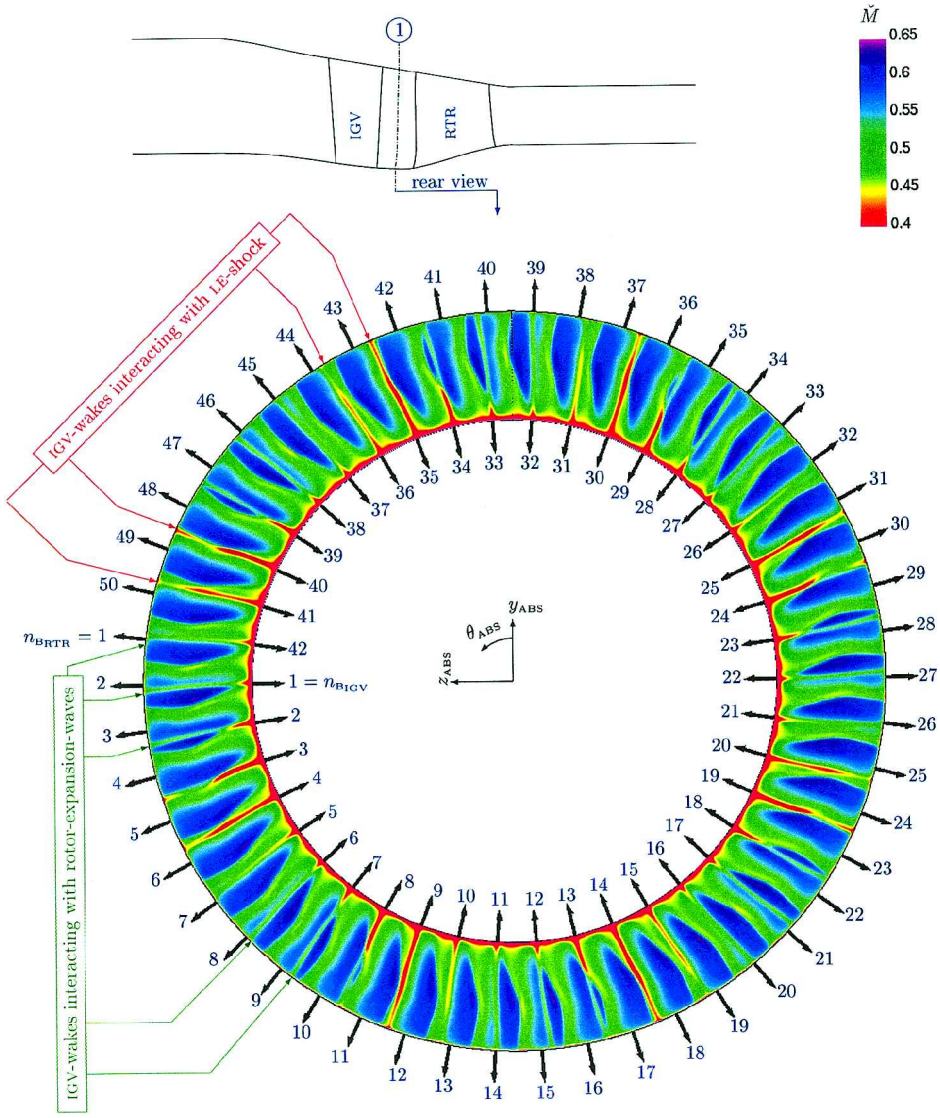

Fig. 9 Instantaneous ($t = 0$) levels of absolute Mach number $\check{M}$ at the IGV/RTR interface of the transonic compressor (rear view, flow coming outward toward the observer); inner radius arrows indicate the azimuthal location of the IGV trailing edges at the hub; outer radius arrows indicate the azimuthal location of the rotor leading edges at the tip (design operating point).

in time derivative is reduced by 1.5–2 orders of magnitude. (This choice defines the number of subiterations at each time step.)

Conclusions

In the present paper, a systematic analysis of the chorochronic periodicity that characterizes the interaction of two turbomachinery blade rows in relative angular motion is presented and applied to the computation of typical turbine and compressor configurations. The main conclusions are as follows.

1) The aerodynamic phenomena observed in the frame of reference of each blade row exhibit, in the absence of aerodynamic instabilities, a traveling wave behavior of known frequency (the blade passing frequency of the adjacent blade row).

2) This traveling wave behavior, where, in a given blade row, each blade observes the same aerodynamic phenomena as the neighboring blade of the same blade row, implies that if at a given meridional position ($[x, R]$) the $t\theta$ signal is described by Fourier series of $t\theta$ harmonics ($[n_t, n_\theta]$), only a few θ harmonics n_θ are nonzero for each n_t. (These nonzero harmonics are easily determined by the number of blades of the two interacting blade rows, the sign of relative rotation, and by n_t.)

3) This result is valid in the frame of reference of each blade row, but with different frequencies in each frame of reference (Doppler shift due to the relative rotation and to the difference in number of blades).

4) When the $t\theta$ series in each frame of reference, as well as the same $t\theta$ signal being observed in both frames of reference are taken into account, a straightforward correspondence is established between the nonzero chorochronic harmonics $[n_{t_1}, n_{\theta_1}]$ and $[n_{t_2}, n_{\theta_2}]$, where corresponding harmonics have the same $n_\theta = n_{\theta_1} = n_{\theta_2}$ and generally (but not invariably) different $n_{t_1} \neq n_{t_2}$. (This relation is easily determined by n_θ, the number of blades of the two interacting blade rows and the sign of relative rotation.)

5) These results allow a mathematically simple (and, as a consequence, straightforward to implement) representation of the computational interface between the two interacting blade rows (chorochronic interface), based on the use of the a priori known nonzero chorochronic harmonics to store and transmit information. (In practice, N_t time harmonics and the corresponding first L_θ nonzero θ harmonics are retained.)

6) An implementation of the preceding results is developed, wherein the flow around a single blade per blade row is discretized and computed using phase-shifted periodicity conditions at the pitchwise boundaries (based on Fourier time series of the signals) and the chorochronic harmonics representation of the interface. (Both t harmonics and $t\theta$ harmonics are computed using a low-storage moving-averages technique developed in the present work.)

7) This implementation was incorporated in a computational methodology (*turbo_3D*), solving the Favre–Reynolds-averaged compressible Navier–Stokes equations with a near-wall wall-normal-free Reynolds-stress model (five mean flow and seven turbulence transport equations). It was then successfully applied to the computation of a subsonic turbine and a transonic compressor, illustrating the ability of the technique to compute rotor/stator interactions with arbitrary pitch ratio between the two interacting blade rows.

Appendix: Moving Averages

The method used for the computation of the time harmonics and the chorochronic harmonics is based on a moving-averages technique that does not require storing time signals, but only their harmonics. This method computes the harmonics iteratively, by applying an appropriate correction at each iteration. The method can be viewed as using a moving window of length equal to the period for computing the integrals.

Time Harmonics

If the fundamental period of the function $F(t)$ is f^{-1}, the Fourier series are[52]

$$F(t) = \Re\left\{\sum_{n_t=0}^{+\infty}[\check{F}(n_t)\exp(i2\pi n_t f t)]\right\} \cong \Re\left\{\sum_{n_t=0}^{N_t}[\check{F}(n_t)\exp(i2\pi n_t f t)]\right\} \tag{A1}$$

where N_t is the number of time-harmonics retained, and the harmonics $\check{F}(n_t)$ ($n_t = 0, 1, \ldots$) are given by the well-known expressions[52]

$$\check{F}(n_t) = C(n_t) f \int_{t_0}^{t_0+f^{-1}} F(t)\exp(-i2\pi n_t f t)\,\mathrm{d}t$$

$$C(0) = 1, \qquad C(n_t) = 2, \qquad n_t = 1, 2, \ldots \tag{A2}$$

where t_0 is an arbitrary initial time. In a moving-averages technique, the harmonics are updated at each time step, so that at time steps n (time ${}^{n}t = [n-1]\Delta t$) and $n+1$ (time ${}^{n+1}t = n\Delta t$)

$$\check{F}\left(n_t; {}^{n}t\right) = C(n_t) f \int_{n+\frac{1}{2}t-f^{-1}}^{n+\frac{1}{2}t} F(t)\exp(-i2\pi n_t f t)\,\mathrm{d}t \cong C(n_t) f \sum_{\ell=n-N_{\mathrm{PP}}+1}^{n}\left[F({}^{\ell}t)\exp\left(-i2\pi n_t f {}^{\ell}t\right)\right]\Delta t$$

$$\check{F}\left(n_t; {}^{n+1}t\right) = C(n_t) f \int_{n+\frac{3}{2}t-f^{-1}}^{n+\frac{3}{2}t} F(t)\exp(-i2\pi n_t f t)\,\mathrm{d}t \cong C(n_t) f \sum_{\ell=n-N_{\mathrm{PP}}+2}^{n+1}\left[F({}^{\ell}t)\exp\left(-i2\pi n_t f {}^{\ell}t\right)\right]\Delta t \tag{A3}$$

where N_{PP} are the instants per period ($N_{\mathrm{PP}}\Delta t = f^{-1}$). The only difference between the integrals (Fig. A1) is that the first contains the interval around ${}^{n+1}t - f^{-1}$ (absent in the second), and the second contains the interval around ${}^{n+1}t$ (absent in the first), so that

$$\check{F}\left(n_t; {}^{n+1}t\right) = \check{F}\left(n_t; {}^{n}t\right) + C(n_t) f \Delta t\left[F({}^{n+1}t) - F\left({}^{n-N_{\mathrm{PP}}+1}t\right)\right]\exp\left(-i2\pi n_t f^{n+1}t\right) \tag{A4}$$

where use was made of the periodicity $\exp(-i2\pi n_t f t) = \exp[-i2\pi n_t f(t \pm f^{-1})]$. Approximating $F({}^{n-N_{\mathrm{PP}}+1}t)$ with Fourier series of the time ${}^{n}t$ harmonics yields the following correction formula for the time ${}^{n+1}t$ harmonics

$$\check{F}\left(n_t; {}^{n+1}t\right) - \check{F}\left(n_t; {}^{n}t\right) = C(n_t) f \Delta t\left\{F({}^{n+1}t) - \Re\left[\sum_{m_t=0}^{N_t}\times\check{F}\left(m_t; {}^{n}t\right)\exp\left(i2\pi m_t f^{n+1}t\right)\right]\right\}\exp\left(-i2\pi n_t f^{n+1}t\right) \tag{A5}$$

Chorochronic Harmonics

The same technique is used for the chorochronic $t\theta$ harmonics. In this case, there is, however, the additional complication that the instantaneous values of $F(t,\theta)$ are only available for a θ sector of $2\pi N_B^{-1}$. For instance, the instantaneous values from which the downstream interface phantoms of blade row $n_{\mathrm{BR}} = 1$ (Fig. 3) are updated are only known for the sector $Q_- Q_+$ (Fig. 3). Therefore, a moving-averages technique, making explicit use of the chorochronic periodicity conditions, was developed. Indeed, the time signal is represented by the $t\theta$ harmonics[53]

$$F(t,\theta) = \sum_{n_t=-\infty}^{+\infty}\sum_{n_\theta=-\infty}^{+\infty}\hat{F}(n_t, n_\theta)\exp(i2\pi n_t f t + i n_\theta\theta) \cong \sum_{n_t=-N_t}^{+N_t}\sum_{n_\theta=-N_\theta}^{+N_\theta}\hat{F}(n_t, n_\theta)\exp(i2\pi n_t f t + i n_\theta\theta) \tag{A6}$$

truncated to N_t and N_θ, respectively. It can be easily shown that the $t\theta$ harmonics are given by the integral

$$\hat{F}(n_t, n_\theta) = \frac{f}{2\pi}\int_{t_0}^{t_0+f^{-1}}\int_{\theta_0}^{\theta_0+2\pi} F(t',\theta')\exp(-i2\pi n_t f t' - i n_\theta\theta')\,\mathrm{d}t'\,\mathrm{d}\theta' = \frac{f}{2\pi}\int_{t_0}^{t_0+f^{-1}}\left\{\left[\sum_{n_B=1}^{N_B}\left(\int_{\theta_0+(n_B-1)(2\pi/N_B)}^{\theta_0+n_B(2\pi/N_B)}\times F(t',\theta')\exp(-i n_\theta\theta')\,\mathrm{d}\theta'\right)\right]\exp(-i2\pi n_t f t')\,\mathrm{d}t'\right\} \tag{A7}$$

where the θ integral in $[0, 2\pi]$ was computed as the sum of N_B integrals over each $2\pi N_B^{-1}$ sector. Each θ integral can be expressed on the reference sector $[\theta_0, \theta_0 + 2\pi N_B^{-1}]$ by the application of the transformation $\theta = \theta' - (n_B - 1)2\pi N_B^{-1}$

$$\int_{\theta_0+(n_B-1)(2\pi/N_B)}^{\theta_0+n_B(2\pi/N_B)} F(t',\theta')\exp(-i n_\theta\theta')\,\mathrm{d}\theta' = \exp\left[-i(n_B-1)n_\theta\frac{2\pi}{N_B}\right]\times\int_{\theta_0}^{\theta_0+2\pi/N_B} F\left[t', \theta + (n_B-1)\frac{2\pi}{N_B}\right]\exp(-i n_\theta\theta)\,\mathrm{d}\theta = \exp\left[-i(n_B-1)n_\theta\frac{2\pi}{N_B}\right]\int_{\theta_0}^{\theta_0+2\pi/N_B}\times F\left[t' + (n_B-1)\frac{\beta_r}{2\pi f}, \theta\right]\exp(-i n_\theta\theta)\,\mathrm{d}\theta \tag{A8}$$

where the chorochronic periodicity conditions [(Eqs. (3)] were used in the last equality. In this way, the θ integral only needs to be evaluated for the reference blade, and the $t\theta$ harmonics under chorochronic periodicity conditions [Eqs. (3)] can be expressed (after some obvious rearrangements in the order of summation and $t\theta$ integrations)

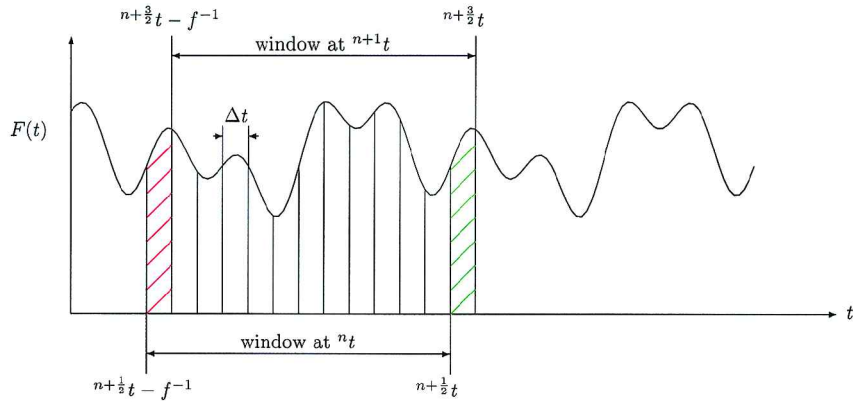

Fig. A1 Moving averages technique for updating harmonics: the red cross-hatched trapeze used [Eqs. (A3)] for the evaluation of the harmonics $\hat{F}(n_t; {}^{n}t)$ is replaced by the green cross-hatched trapeze when computing [Eqs. (A3)] the harmonics $\hat{F}(n_t; {}^{n+1}t)$ (N_{PP} = 12).

$$\hat{F}(n_t, n_\theta) = \frac{f}{2\pi} \sum_{n_B=1}^{N_B} \left\{ \exp\left[-i(n_B-1)n_\theta \frac{2\pi}{N_B}\right] \times \left[\int_{\theta_0}^{\theta_0 + 2\pi/N_B} \left(\int_{t_0}^{t_0 + f^{-1}} F\left[t' + (n_B-1)\frac{\beta_r}{2\pi f}, \theta\right] \times \exp(-i2\pi n_t f t')\, \mathrm{d}t' \right) \exp(-in_\theta\theta)\, \mathrm{d}\theta \right] \right\} \tag{A9}$$

Finally, by application of the transformation $2\pi f t = 2\pi f t' + (n_B - 1)\beta_r$, the following expression is obtained after some simple manipulations, where the well-known property applies that, for a t-periodic function $G(t)$, the integral over a period is independent of the window used (as long as the length of the window is equal to the period)

$$G(t) = G(t + f^{-1}) \quad \forall t \Longleftarrow \int_{t_0}^{t_0 + f^{-1}} G(t)\, \mathrm{d}t = \int_{t_1}^{t_1 + f^{-1}} G(t)\, \mathrm{d}t, \qquad \forall t_0, \quad t_1$$

we then get

$$\hat{F}(n_t, n_\theta) = \frac{f}{2\pi} \left(\sum_{n_B=1}^{N_B} \exp\left\{ -i(n_B-1)\left[-n_t\beta_r + n_\theta \frac{2\pi}{N_B}\right]\right\}\right) \times \left[\int_{t_0}^{t_0 + f^{-1}} \int_{\theta_0}^{\theta_0 + 2\pi/N_B} F(t,\theta) \exp(-i2\pi n_t f t - in_\theta\theta)\, \mathrm{d}t\, \mathrm{d}\theta \right] \tag{A10}$$

With the expressions for β_r [Eqs. (2)] and for $n_\theta(n_t, \ell_\theta)$ [Eqs. (8)], it follows that the multiplicative constant before the integrals [Eq. (A10)] is equal to

$$\frac{f}{2\pi} \left(\sum_{n_B=1}^{N_B} \exp\left\{ -i(n_B-1)\left[-n_t\beta_r + n_\theta \frac{2\pi}{N_B}\right]\right\}\right) = \frac{f}{2\pi} \left(\sum_{n_B=1}^{N_B} \exp[-i(n_B-1)2\pi\ell_\theta] \right) = \frac{f}{2\pi} \sum_{n_B=1}^{N_B} 1 = \frac{f}{2\pi} N_B, \qquad \forall n_t, \quad \ell_\theta \tag{A11}$$

The final result is that under chorochronic periodicity conditions [Eqs. (2), (3), and (8)] the interface $t\theta$ harmonics can be computed on a single $2\pi N_B^{-1}$ sector, simply by multiplying the integral by the number of blades N_B

$$\text{[Eqs. (2), (3), and (8)]} \Rightarrow \hat{F}(n_t, n_\theta) = \frac{f}{2\pi} \int_{t_0}^{t_0 + f^{-1}} \int_{\theta_0}^{\theta_0 + 2\pi} \times F(t,\theta) \exp(-i2\pi n_t f t - in_\theta\theta)\, \mathrm{d}t\, \mathrm{d}\theta = \frac{f}{2\pi} N_B \int_{t_0}^{t_0 + f^{-1}} \times \int_{\theta_0}^{\theta_0 + 2\pi/N_B} F(t,\theta) \exp(-i2\pi n_t f t - in_\theta\theta)\, \mathrm{d}t\, \mathrm{d}\theta \tag{A12}$$

The preceding relation allows a straightforward application of the moving-averages technique for the chorochronic harmonics. Indeed, Eq. (A12) can be written

$$\hat{F}(n_t, n_\theta) = \frac{f}{2\pi} \int_{t_0}^{t_0 + f^{-1}} I_\theta(t;\, f, n_\theta, \theta_0, N_B) \exp(-i2\pi n_t f t)\, \mathrm{d}t$$

$$I_\theta = \left[N_B \int_{\theta_0}^{\theta_0 + 2\pi/N_B} F(t,\theta) \exp(-in_\theta\theta)\, \mathrm{d}\theta \right] \in \mathbb{C} \tag{A13}$$

Computing the chorochronic harmonics $\hat{F}(n_t, n_\theta)$ is equivalent to computing time harmonics of the function $I_\theta(t;\, f, n_\theta, \theta_0, N_B)$ by applying the moving-averages technique [(Eq. (A5)], and it is easy to show that the following correction formula is applicable

$$\hat{F}\left(n_t, n_\theta; {}^{n+1}t\right) - \hat{F}\left(n_t, n_\theta; {}^{n}t\right) = \frac{f}{2\pi} N_B \Delta t \exp\left(-i2\pi n_t f\, {}^{n+1}t\right) \left\{ \int_{\theta_0}^{\theta_0 + 2\pi/N_B} \left[F({}^{n+1}t, \theta) - \left(\sum_{m_t=-N_t}^{N_t} \sum_{m_\theta=-N_\theta}^{N_\theta} \hat{F}\left(m_t, m_\theta; {}^{n}t\right) \times \exp\left(i2\pi m_t f^{n+1}t + im_\theta\theta\right)\right)\right] \exp(-in_\theta\theta)\, \mathrm{d}\theta \right\} \tag{A14}$$

valid for all nonzero chorochronic harmonics $n_\theta = n_\theta[n_t, \ell_\theta]$ [Eqs. (8)].

Acknowledgments

The computations presented were run at the Institut pour le Développement des Ressources en Informatique Scientifique, where computer resources were made available by the Comité Scientifique. Authors are listed alphabetically.

References

[1] Kerrebrock, J. L., and Mikolajczak, A. A., "Intra-Stator Transport of Rotor Wakes and Its Effect on Compressor Performance," *Journal of Engineering for Power*, Vol. 92, Oct. 1970, pp. 359–368.

[2]Zierke, W. L., and Okiishi, T. H., "Measurement and Analysis of Total Pressure Unsteadiness Data from an Axial Flow Compresor Stage," *Journal of Engineering for Power*, Vol. 104, April 1982, pp. 479–488.

[3]Favrat, D., and Suter, P., "Interaction of the Rotor–Blade Shock-Waves in Supersonic Compressors with Upstream Stator Vanes," *Journal of Engineering for Power*, Vol. 100, Jan. 1978, pp. 140–147.

[4]Sharma, O. P., Picket, G. F., and Ni, R. H., "Assessment of Unsteady Flows in Turbines," *Journal of Turbomachinery*, Vol. 114, Jan. 1992, pp. 79–90.

[5]Dawes, W. N., "A Simulation of the Unsteady Interaction of a Centrifugal Impeller with Its Vanes Diffuser: Flow Analysis," *Journal of Turbomachinery*, Vol. 117, April 1995, pp. 213–222.

[6]Saxer, A. P., and Felici, H. M., "Numerical Analysis of Three-Dimensional Unsteady Hot Streak Migration and Shock Interaction in a Turbine Stage," *Journal of Turbomachinery*, Vol. 118, April 1996, pp. 268–277.

[7]Janus, J. M., Horstman, H. Z., and Whitfield, D. L., "Unsteady Flowfield Simulation of Ducted Propfan Configurations," *Journal of Propulsion and Power*, Vol. 15, No. 1, 1999, pp. 64–72.

[8]Höhn, W., and Heinig, K., "Numerical and Experimental Investigation of Unsteady Flow Interaction in a Low-Pressure Multistage Turbine," *Journal of Turbomachinery*, Vol. 122, Oct. 2000, pp. 628–633.

[9]Sondak, D. L., and Dorney, D. J., "Simulation of Coupled Unsteady Flow and Heat Conduction in a Turbine Stage," *Journal of Propulsion and Power*, Vol. 16, No. 6, 2000, pp. 1141–1148.

[10]Dorney, D. J., and Sondak, D. L., "Effects of Tip-Clearance on Hot Streak Migration in a High-Subsonic Single-Stage Turbine," *Journal of Turbomachinery*, Vol. 122, Oct. 2000, pp. 613–620.

[11]Dénos, R., Arts, T., Paniagua, G., Michelassi, V., and Martelli, F., "Investigation of the Unsteady Rotor Aerodynamics in a Transonic Turbine Stage," *Journal of Turbomachinery*, Vol. 123, Jan. 2001, pp. 81–80.

[12]Dunn, M. G., "Convective Heat Transfer and Aerodynamics in Axial Flow Turbines," *Journal of Turbomachinery*, Vol. 123, Oct. 2001, pp. 637–686.

[13]Arnone, A., and Pacciani, R, "Rotor–Stator Interaction Analysis Using the Navier–Stokes Equations and a Multigrid Method," *Journal of Turbomachinery*, Vol. 118, Oct. 1996, pp. 679–689.

[14]Tyler, J. M., and Sofrin, T. G., "Axial Flow Compressor Noise Studies," *SAE Transactions*, Vol. 70, 1962, pp. 309–332.

[15]Erdos, J. I., Alzner, E., and McNally, W., "Numerical Solution of Periodic Transonic Flow Through a Fan Stage," *AIAA Journal*, Vol. 15, No. 11, 1977, pp. 1559–1568.

[16]Koya, M., and Kotake, S., "Numerical Analysis of Fully Three-Dimensional Periodic Flows Through a Turbine Stage," *Journal of Engineering for Gas Turbines and Power*, Vol. 107, Oct. 1985, pp. 945–952.

[17]Lewis, J. P., Delaney, R. A., and Hall, E. J., "Numerical Prediction of Turbine Vane–Blade Aerodynamic Interaction," *Journal of Turbomachinery*, Vol. 111, Oct. 1989, pp. 387–393.

[18]Giles, M. B., "Stator/Rotor Interaction in a Transonic Turbine," *Journal of Propulsion and Power*, Vol. 6, No. 5, 1990, pp. 621–627.

[19]Krouthén, B., and Giles, M. B., "Numerical Investigation of Hot Streaks in Turbines," *Journal of Propulsion and Power*, Vol. 6, No. 6, 1990, pp. 769–776.

[20]Abhari, R. S., Guenette, G. R., Epstein, A. H., and Giles, M. B., "Comparison of Time-Resolved Turbine Rotor Blade Heat Transfer Measurements and Numerical Calculations," *Journal of Turbomachinery*, Vol. 114, Oct. 1992, pp. 818–827.

[21]Hah, C., Puterbaugh, S. L., and Copenhaver, W. W., "Unsteady Aerodynamic Flow Phenomena in a Transonic Compressor Stage," *Journal of Propulsion and Power*, Vol. 13, No. 3, 1997, pp. 329–333; also AIAA paper 93-1868, 1993.

[22]Gallus, H. E., Zeschky, J., and Hah, C., "Endwall and Unsteady Flow Phenomena in an Axial Turbine Stage," *Journal of Turbomachinery*, Vol. 117, Oct. 1995, pp. 562–570.

[23]Jung, R. J., Mayer, J. F., and Stetter, H., "Simulation of 3D-Unsteady Stator/Rotor Interaction in Turbomachinery Stages of Arbitrary Pitch Ratio," American Society of Mechanical Engineers, ASME Paper 96-GT-069, 1996.

[24]Jung, R. J., Mayer, J. F., and Stetter, H., "Prediction of 3D Unsteady Flow in an Air Turbine and a Transonic Compressor Including Blade Gap Flow and Blade Row Interaction," American Society of Mechanical Engineers, ASME Paper 97-GT-094, 1997.

[25]Walraevens, R. E., Gallus, H. E., Jung, A. R., Mayer, J. F., and Stetter, H., "Experimental and Computational Study of the Unsteady Flow in an $1\frac{1}{2}$ stage Axial Turbine with Emphasis on the Secondary Flow in the Second Stator," American Society of Mechanical Engineers, ASME Paper 98-GT-254, 1998.

[26]von Hoyningen-Huene, M., and Jung, A. R., "Comparison of Different Acceleration Techniques and Methods for Periodic Boundary Treatment in Unsteady Turbine Stage Flow Simulations," *Journal of Turbomachinery*, Vol. 122, April 2000, pp. 234–246.

[27]Volmar, T. W., Brouillet, B., Gallus, H. E., and Benetschik, H., "Time-Accurate Three-Dimensional Navier–Stokes Analysis of One- and-One-Half-Stage Axial-Flow Turbine," *Journal of Propulsion and Power*, Vol. 16, No. 2, 2000, pp. 327–335.

[28]Reinmöller, U., Stephan, B., Schmidt, S., and Niehuis, R., "Clocking Effects in a $1\frac{1}{2}$ stage Axial Turbine—Steady and Unsteady Experimental Investigations Supported by Numerical Simulations," *Journal of Turbomachinery*, Vol. 124, Jan. 2002, pp. 52–60.

[29]Gerolymos, G. A., and Chapin, V. C., "Generalized Expression of Chorochronic Periodicity in Turbomachinery Blade-Row Interaction," *Rech. Aérosp.*, Vol. 1991. 5, No. 5, 1991, pp. 69–73.

[30]Kemp, N. H., and Sears, W. R., "Aerodynamic Interference Between Moving Blade-Rows," *Journal of the Aeronautical Sciences*, Vol. 20, No. 9, 1953, pp. 585–597, 612.

[31]Ning, W., and He, L., "Some Modeling Issues on Trailing-Edge Vortex Shedding," *AIAA Journal*, Vol. 39, No. 5, 2001, pp. 787–793.

[32]Sondak, D. L., and Dorney, D. J., "Simulation of Vortex Shedding in a Turbine Stage," *Journal of Turbomachinery*, Vol. 121, July 1999, pp. 428–435.

[33]He, L., "Computational Study of Rotating Stall Inception in Axial Compressors," *Journal of Propulsion and Power*, Vol. 13, No. 1, 1997, pp. 31–38.

[34]Saxer-Felici, H. M., Saxer, A. P., Inderbitzin, A., and Gyarmathy, G., "Prediction and Measurement of Rotating Stall Cells in an Axial Compressor," *Journal of Turbomachinery*, Vol. 121, April 1999, pp. 365–375.

[35]Saxer-Felici, H. M., Saxer, A. P., Inderbitzin, A., and Gyarmathy, G., "Numerical and Experimental Study of Rotating Stall in an Axial Compressor Stage," *AIAA Journal*, Vol. 38, No. 7, 2000, pp. 1132–1141.

[36]He, L., "Method of Simulating Unsteady Turbomachinery Flows with Multiple Perturbations," *AIAA Journal*, Vol. 30, No. 11, 1992, pp. 2730–2735.

[37]Giles, M. B., "Calculation of Unsteady Wake/Rotor Interaction," *Journal of Propulsion and Power*, Vol. 4, No. 4, 1988, pp. 356–362.

[38]Walraevens, R. E., and Gallus, H. E., "Stator–Rotor–Stator Interaction in an Axial Flow Turbine and Its Influence on Loss Mechanisms," *AGARD Conference Proceedings*, Vol. 571, 1996, pp. 39.1–39.14.

[39]Haugeard, R., "Aérodynamique Tridimensionnelle Instationnaire des Turbomachines Linéarisée en Temps," Ph.D. Dissertation, Univ. Pierre-et-Marie-Curie, Paris, Jan. 1996.

[40]Gerolymos, G. A., Tsanga, G., and Vallet, I., "Near-Wall k–ε Computation of Transonic Turbomachinery Flows with Tip Clearance," *AIAA Journal*, Vol. 36, No. 10, 1998, pp. 1769–1777.

[41]Gerolymos, G. A., and Hanisch, C., "Multistage Three-Dimensional Navier–Stokes Computation of Off-Design Operation of a 4-Stage Turbine," *IMechE Journal of Power and Energy*, Vol. 213, 1999, pp. 243–261.

[42]Zienkiewicz, O. C., *The Finite Element Method*, McGraw–Hill, New York, 1977, pp. 164–168.

[43]Gerolymos, G. A., and Vallet, I., "Wall-Normal-Free Near-Wall Reynolds-Stress Closure for Three-Dimensional Compressible Separated Flows," *AIAA Journal*, Vol. 39, No. 10, 2001, pp. 1833–1842.

[44]Gerolymos, G. A., and Vallet, I., "'Wall-Normal-Free Reynolds-Stress Model for Compressible Rotating Flows Applied to Turbomachinery," *AIAA Journal*, Vol. 40, No. 2, 2002, pp. 199–208.

[45]Gerolymos, G. A., Neubauer, J., Sharma, V. C., and Vallet, I., "Improved Prediction of Turbomachinery Flows Using Near-Wall Reynolds-Stress Model," *Journal of Turbomachinery*, Vol. 124, Jan. 2002, pp. 86–99.

[46]Gerolymos, G. A., and Tsanga, G., "Biharmonic Three-Dimensional Grid Generation for Axial Turbomachinery with Tip Clearance," *Journal of Propulsion and Power*, Vol. 15, No. 3, 1999, pp. 476–479.

[47]Gerolymos, G. A., and Vallet, I., "Tip-Clearance and Secondary Flows in a Transonic Compressor Rotor," *Journal of Turbomachinery*, Vol. 121, Oct. 1999, pp. 751–762.

[48]Gerolymos, G. A., and Vallet, I., "Implicit Computation of the Three-Dimensional Compressible Navier–Stokes Equations using k–ε Turbulence Closure," *AIAA Journal*, Vol. 34, No. 7, 1996, pp. 1320, 1321.

[49]Chassaing, J. C., "Aérodynamique Tridimensionnelle et Aéroélasticité Nonlinéaire et Linéarisée en Temps," Ph.D. Dissertation, Univ. Pierre-et-Marie-Curie, Paris, Jan. 2002.

[50]Shannon, C. E., "Communications in the Presence of Noise," *Proceedings of the IRE*, Vol. 37, 1949, pp. 10–21.

[51]Levine, P., "Two-Dimensional Inflow Conditions for a Supersonic Compressor with Curved Blades," *Journal of Applied Mechanics*, Vol. 24, 1957, pp. 165–169.

[52]Harris, J. W., and Stocker, H., *Handbook of Mathematics and Computational Science*, Springer-Verlag, New York, 1998, p. 698.

[53]Smirnov, V., *Cours de Mathématiques Supérieures*, Vol. 2, Editions MIR, Moscow, 1970, pp. 527–529.